HHS Public Access

Author manuscript

Cell Rep. Author manuscript; available in PMC 2024 July 02.

Published in final edited form as:

Cell Rep. 2024 June 25; 43(6): 114286. doi:10.1016/j.celrep.2024.114286.

CRACD Loss Induces Neuroendocrine Cell Plasticity of Lung Adenocarcinoma

Bongjun Kim[1,†], **Shengzhe Zhang**[1], **Yuanjian Huang**[1], **Kyung-Pil Ko**[1], **Youn-Sang Jung**[1], **Jinho Jang**[1], **Gengyi Zou**[1], **Jie Zhang**[1], **Sohee Jun**[1], **Kee-Beom Kim**[2,3], **Kwon-Sik Park**[2], **Jae-Il Park**[1,4,5,†]

[1]Department of Experimental Radiation Oncology, Division of Radiation Oncology, The University of Texas MD Anderson Cancer Center, Houston, TX 77030, USA

[2]Department of Microbiology, Immunology, and Cancer Biology, University of Virginia School of Medicine, Charlottesville, VA 22908, USA

[3]BK21 FOUR KNU Creative BioResearch Group, School of Life Sciences, Kyungpook National, University, Daegu, 41566, Republic of Korea

[4]Graduate School of Biomedical Sciences, The University of Texas MD Anderson Cancer Center, Houston, TX 77030, USA

[5]Program in Genetics and Epigenetics, The University of Texas MD Anderson Cancer Center, Houston, TX 77030, USA

Summary

Tumor cell plasticity contributes to intratumoral heterogeneity and therapy resistance. Through cell plasticity, some lung adenocarcinoma (LUAD) cells transform into neuroendocrine (NE) tumor cells. However, the mechanisms of NE cell plasticity remain unclear. CRACD, a capping protein inhibitor, is frequently inactivated in cancers. *CRACD* knock-out (KO) is sufficient to de-repress NE-related gene expression in the pulmonary epithelium and LUAD cells. In LUAD mouse models, *Cracd* KO increases intratumoral heterogeneity with NE gene expression. Single-cell transcriptomic analysis showed that *Cracd* KO-induced NE cell plasticity is associated with cell de-differentiation and stemness-related pathway activation. The single-cell transcriptomic

[†]Lead contact: Bongjun Kim (bkim6@mdanderseon.org) and Jae-Il Park (jaeil@mdanderson.org), Fax: 713-794-5369.

Author contributions

B.K.: Conceptualization, Methodology, Software, Formal analysis, Investigation, Data Curation, Writing - Original Draft, Writing - Review & Editing, Visualization
S.Z.: Methodology, Formal analysis, Investigation, Data Curation
Y.H.: Investigation, Software
K.-P.K.: Investigation
Y.-S.J.: Investigation
J.J.: Software
G.Z.: Validation, Formal analysis, Investigation
J.Z.: Investigation
S.J.: Investigation
K.-B.K.: Resources
K.-S.P.: Resources
J.-I.P.: Conceptualization, Methodology, Formal analysis, Writing - Original Draft, Writing - Review & Editing, Visualization, Supervision, Project administration, Funding acquisition

Declaration of interests

The authors declare no competing interests.

analysis of LUAD patient tumors recapitulates that the distinct LUAD NE cell cluster expressing NE genes is co-enriched with impaired actin remodeling. This study reveals the crucial role of CRACD in restricting NE cell plasticity that induces cell de-differentiation of LUAD.

Keywords

Cell plasticity; neuroendocrine cell plasticity; CRACD; CRAD; KIAA1211; lung adenocarcinoma; cell plasticity; cell de-differentiation; tumor heterogeneity; therapy resistance; single-cell transcriptomics

Introduction

Cell plasticity, a process changing cell fate or state [1–3], plays pivotal roles in development, tissue homeostasis, and regeneration. During development, embryonic progenitor cells change their cell fate [2,3]. Upon cell intrinsic or extrinsic signaling cues, terminally differentiated cells undergo cell plasticity via de-differentiation or trans-differentiation, contributing to the homeostasis and regeneration of many tissues [4–10].

Cell plasticity also plays a crucial role in tumorigenesis [11,12]. Tumor cell plasticity contributes to tumor progression, intratumoral heterogeneity, and therapy resistance [11–13]. In LUAD, tumor cell plasticity changes the cancer subtype [12,14,15]. For example, during EGFR-targeted therapies, *EGFR* mutant LUAD tumor cells transform into NE tumor cells [16,17]. A $Kras^{G12C}$ inhibitor, AMG510, induces tumor cell plasticity, converting $KRAS^{G12C}$ mutant LUAD tumor cells into squamous cancer cells [18]. The ALK inhibitor, crizotinib, changes *ALK*-mutant LUAD tumor cells into small cell lung cancer (SCLC) [19]. NE cell plasticity was also observed in melanoma [20], pancreatic adenocarcinoma [21] , and prostate cancer [22]. However, the mechanisms of NE cell plasticity of LUAD remain elusive.

In this study, leveraging genetically engineered mouse models, organoids, and single-cell transcriptomics, we found that CRACD tumor suppressor serves as a gatekeeper restricting NE cell plasticity, which might be implicated in LUAD's therapy resistance and tumor cell heterogeneity.

Results

Cracd KO generates NE-like pulmonary epithelial cells.

Previously, we identified the CRACD (Capping protein inhibiting Regulator of Actin Dynamics, also known as CRAD/KIAA1211) tumor suppressor, which promotes actin polymerization by binding and inhibiting capping proteins to promote actin polymerization [23]. Interestingly, we observed hyperplastic lesions in the lungs of *Cracd* KO mice [23]. This observation led us to hypothesize that CRACD loss may drive NE-like cell plasticity in the lung. To test this, we examined *Cracd* KO mouse lung tissues. Unlike *Cracd* wild-type (WT), *Cracd* KO lung tissues showed NE-like hyperplasia in the bronchiolar airway and alveoli (Fig. 1A). Immunofluorescent (IF) staining confirmed the proliferative nature of this NE-like cell mass, as indicated by MKI67+, a marker for cell proliferation. Furthermore, the mass expressed several NE markers, including KRT19, SYP, CGRP, CHGA, and ASCL1 (Fig.

1B). It is noteworthy that *Cracd* KO alone failed to develop lung tumors in mice [23]. We also assessed the expression of NE markers in lung organoids (LOs) derived from pulmonary epithelial cells isolated from murine lung tissues (*Cracd* WT vs. KO) [24] (Fig. 1C, D; fig. S1A). We confirmed the generation of three different types of LOs: alveolar (HOPX [a marker for alveolar type I cells] and SPC [a marker for alveolar type II cells]), bronchiolar (Ac-Tub [a marker for ciliated cells], SCGB1A1 [club cells]), and bronchioalveolar (HOPX, SPC, Ac-Tub, SCGB1A1) types (Fig. 1E). Compared to *Cracd* WT LOs, *Cracd* KO LOs exhibited increased expression of NE markers, CHGA and CGRP, in both bronchiolar and alveolar LOs (Fig. 1F, G). Intriguingly, non-NE cells (AT1, AT2, and club cells) showed CGRP expression in *Cracd* KO LOs (fig. S1B-D). These results suggest that CRACD loss is sufficient to induce NE-like features in the pulmonary epithelium.

NE plasticity is associated with de-differentiation of pulmonary epithelial cells.

To elucidate the mechanisms of *Cracd* KO-induced NE marker expression, we employed single-cell transcriptomics. We isolated pulmonary epithelial cells from mouse lung tissues (*Cracd* WT or KO) and performed single-cell RNA sequencing (scRNA-seq) (fig. S2). Using unsupervised clustering and annotations, we identified each pulmonary epithelial cell type (Fig. 2A-C; fig. S2, Table S2). Consistent with the IF results (Fig. 1), the *Cracd* KO lung tissue exhibited a relatively higher expression of NE- and SCLC-related genes (Fig. 2D). In the normal (*Cracd* WT) lung, the expression of NE markers (*Ascl1, ChgA, Calca, Ncam1, Syp*, and *Uchl1*) was enriched in NE cells. A few ciliated ('Ciliated-1') and club cells also expressed several NE markers (*Uchl1*, *Syp*, and *Ncam1*; *Uchl1*, *Syp*, *Ncam1, Calca, ChgA, and Ascl1*). Compared to WT, *Cracd* KO lung tissues showed the upregulation of NE markers in NE cells, whereas Club and Ciliated-1 cells did not exhibit the upregulation of NE markers. However, a few of the AT cells (AT2-1, 2, 3, 4, and 5 cell clusters) displayed the expression of NE markers, while NE markers were not detected in AT1 cells of *Cracd* KO lung (Fig. 2D).

Since cell plasticity is associated with cell de-differentiation or transdifferentiation [25], we evaluated the impact of *Cracd* KO on cell differentiation and de-differentiation states by using the CytoTRACE package that infers relative cell differentiation states by RNA content [26]. Notably, the *Cracd* KO AT2 clusters (AT2-1~6 cell clusters) displayed significantly less-differentiated states compared to those of *Cracd* WT (Fig. 2E). To determine the signaling pathways involved in *Cracd* KO-induced NE cell plasticity, we conducted fGSEA (fast Geneset Enrichment Analysis) and found that cell stemness-related gene signatures, including OCT4, and NANOG targets (Table S3) [27], were highly enriched in the AT2 cell clusters of the *Cracd* KO lung tissues compared to WT (Fig. 2F), which was shown in the dot and feature plots (Fig. 2G, H).

CRACD depletion induces NE plasticity of LUAD

Having observed NE-like features in *Cracd* KO lung, we investigated whether CRACD depletion also induces NE marker expression in non-NE tumor cells, particularly LUAD cells. We introduced CRACD shRNA into murine (KP-1, derived from *Kras*^{G12D}; *Trp53* KO mouse LUAD tumors) [28] and human (A549) LUAD cell lines. Compared to control cells, we found that CRACD depletion upregulated the expression of NE markers in KP-1 and A549

cells (fig. S3A-D). Additionally, enhanced CGRP expression by shCRACD was rescued by ectopic expression of CRACD (fig. S3E). Moreover, CRACD depletion reduced the cytoplasmic-to-nuclear ratio with the loss of F-actin stress fibers (fig. S3F, G), confirming the role of CRACD in maintaining the actin polymerization [23].

Next, we determined the impact of CRACD loss on the plasticity of LUAD tumor cells in vivo. We employed two approaches to genetically ablate *Cracd* alleles in vivo: CRISPR-based somatic gene targeting [29] and germline deletion. For somatic engineering, we administered adenovirus harboring Cas9-sgLacZ-Cre (control) or Cas9-sgCracd-Cre into KP (*Kras*$^{G12D/WT}$; *Trp53*$^{f/f\ (floxed/floxed)}$) mice, a LUAD mice model, via intratracheal instillation (Fig. 3A). Twelve weeks after adenovirus treatment, we collected lung tissues for tumor analyses. Compared to *Cracd* WT KP-induced LUAD (control), *Cracd* KO KP tumors exhibited significant heterogeneity in tumor cell morphology (Fig. 3B, C, fig. S4A). Moreover, unlike *Cracd* WT KP LUAD, where NE markers were rarely expressed, *Cracd* KO KP tumors showed the expression of NE markers, such as CHGA, CGRP, and ASCL1 (Fig. 3D, E). We confirmed that the NE-marker expressing *Cracd* KO KP cells are tumor cells by performing IF staining for E-Cadherin (Fig. 3E). Additionally, *Cracd* KO tumor cells showed disrupted actin cytoskeleton (fig. S4B). To complement the somatic engineering, we also established the *Cracd* KO (heterozygous and homozygous); *Kras*^{G12D}; *Trp53*$^{f/f}$ (CKP) compound strain. To induce LUAD development, we administered Cre recombinase-expressing adenovirus (Ad-Cre) to KP (control) and CKP mice via intratracheal instillation. Twelve weeks after administration, we examined lung tumors (Fig. 3F). Consistent with the results of somatic engineering, KP tumors carrying the germline mutation of *Cracd* exhibited marked expression of CHGA, CGRP, NEUROD1, and ASCL1 and disrupted actin structure, while *Cracd* WT KP tumors did not (Fig. 3G, fig. S4C, D). Moreover, both *Cracd* homozygous KO (−/−) and heterozygous (+/−) tumors showed increased intratumoral heterogeneity (Fig. 3H, I). In line with the stemness-like features of the *Cracd* KO lung tumors (Fig. 2E-H), somatic engineering or germline deletion of *Cracd* in LUAD was sufficient to induce the expression of SOX2 and OCT4, while the control LUAD tumors (*Cracd* WT) did not express SOX2 and OCT4 (fig. S4E, F). Of note, NANOG was not detected in both *Cracd* WT and KO LUAD tumors (fig. S4G). These results suggest that CRACD loss is sufficient to de-repress NE-related genes and increase intratumoral heterogeneity in LUAD.

Pathological relevance of NE plasticity to human LUAD

To assess the pathological relevance of the NE cell plasticity and cell de-differentiation to LUAD, we analyzed scRNA-seq datasets of non-small cell lung cancer (NSCLC) patient tumor samples [30]. We re-analyze the pre-processed dataset of epithelial compartments consisting of 342 datasets (90,243 tumor cells) and refined the clusters into different types of tumor cells, including LUAD (mitotic, EMT [epithelial-mesenchymal transition], and MSLN [*MSLN* high]), LUAD NE1-3 (neuroendocrine), and lung squamous cell cancer (LUSC) cells (mitotic and EMT) (Fig. 4A), followed by the original code (https://doi.org/10.5281/zenodo.6411867) [30]. We then determined whether NE-related genes were co-expressed with stemness-related genes in LUAD. Among all clusters, the LUAD NE1 cell cluster exhibited a high NE score, including NE-related genes (*CHGA*, *INSM1*, *SYP*,

and *ASCL1*) and stemness-related genes (target genes of SOX2, OCT4, and NANOG and stemness genes enriched in embryonic stem cells [ES]) (Fig. 4B, Table S3) [27], which is consistent with the results from the *Cracd* KO lung scRNA-seq analysis (Fig. 2F-H). The LUAD NE2 cluster also showed relatively less differentiated status (fig. S5A). Since CRACD loss impairs actin remodeling and induces NE cell plasticity, we asked whether the LUAD NE1 cell cluster exhibited the disrupted actin pathway. Indeed, fGSEA analysis showed that actin remodeling-related pathways were relatively decreased in the LUAD NE1 clusters compared to LUAD non-NE clusters (LUAD, LUAD mitotic, LUAD EMT, and LUAD MSLN) (Fig. 4C, D). Since CRACD negatively regulates the WNT signaling [23,31], we also examined the effect of *Cracd* KO on WNT signaling. However, the WNT pathway target genes were marginally increased in *Cracd* KO lung compared to WT (fig. S5B). Similarly, the expression of WNT signaling target genes was rarely altered in LUAD NE1 clusters compared to other clusters (fig. S5C). Interestingly, CRACD depletion decreased E-Cadherin, an epithelial marker, and elevated Vimentin and N-Cadherin, mesenchymal markers, in KP-1 and A549 cells (fig. S3C, D), and promoted tumor sphere formation and cell proliferation (fig. S5D-K). CRACD depletion also increased cell migration of KP-1 but not A549 cells (fig. S5L-O). Furthermore, the germline or conditional ablation of the *Cracd* alleles was sufficient to induce epithelial-mesenchymal plasticity (EMP) features in KP LUAD mouse models (fig. S6). In line with this, the LUAD NE1 and NE3 clusters of human LUAD exhibited EMP characteristics (fig. S7). EMT and EMP are related to chemotherapy resistance [12,32–35]. We observed that CRACD-depleted KP-1 and A549 cells showed relatively higher chemotherapy resistance to certain cancer drugs compared to the control cells (fig. S8). These results suggest that NE cell plasticity is associated with cell de-differentiation of LUAD, potentially related to EMP and chemotherapy resistance.

Discussion

The underlying mechanisms of NE cell plasticity in LUAD have yet to be fully understood. We herein found that the loss of CRACD tumor suppressor was sufficient to de-repress NE-related genes in organoids and mice. Single-cell transcriptomic analysis showed that *Cracd* KO upregulates NE-related genes primarily in AT2 pulmonary epithelial cells, accompanied by an increased cell de-differentiation state. In LUAD mouse models, *Cracd* KO increases intratumoral heterogeneity with the upregulation of NE markers. Single-cell transcriptomes of LUAD patient tumors identified the distinct LUAD cell cluster specifically enriched with NE genes, cell stemness pathways, and impaired actin remodeling.

Tumor cell plasticity is implicated in tumor progression, intratumoral heterogeneity, and therapy resistance [11,12,32]. NE cell plasticity has been observed in lung and prostate cancer as an outcome of cancer therapy [14,17,36]. Our study found that NE cell plasticity is associated with cell de-differentiation of pulmonary epithelial and LUAD tumor cells. The genetic ablation of *Cracd* alone was sufficient to induce a less differentiation state of cells (Fig. 2E). Moreover, cell stemness-related pathways were activated in *Cracd* KO pulmonary epithelial cells (Fig. 2F-H). Analysis of human LUAD single-cell transcriptomes also showed co-expression of NE and stemness-related genes (Fig. 4B). These data suggest that NE cell plasticity is likely driven or accompanied by cell de-differentiation, implying the acquisition of cell stemness through NE cell plasticity. Cell stemness is characterized by two

major features: cellular heterogeneity generation and self-renewal [37]. Thus, such acquired cell stemness might explain why NE cell plasticity increases intratumoral heterogeneity observed in *Cracd* KO LUAD tumors (Fig. 3). Similarly, since tumor cell plasticity also contributes to therapy resistance [11,12], CRACD inactivation-induced NE cell plasticity might generate therapy-resistant tumor cells. Indeed, CRACD-depleted LUAD cells exhibited EMP and LUAD chemotherapy resistance (fig.S3, 6, 8). The NE-like cell clusters of patients' LUAD tumors were also enriched with EMP (fig. S7), which implies the possible connection between NE cell plasticity and LUAD therapy resistance. Given that tumor cell plasticity is one of the hallmarks of cancer [38], targeting NE cell plasticity would be an alternative option for overcoming the therapy resistance of LUAD or LUAD NE.

The *CRACD/KIAA1211* gene is frequently inactivated in SCLC [39–42]. Intriguingly, we observed that CRACD deficiency increases tumor heterogeneity and accelerates SCLC tumorigenesis [43], which somehow agrees with our finding of CRACD loss-induced NE cell plasticity since SCLC tumor cells exhibit NE features. However, the specific mechanisms by which CRACD loss-of-function takes place in LUAD remain to be determined. In colorectal cancer, CRACD inactivation occurs through transcriptional downregulation (via promoter hypermethylation) or genetic mutations (missense and nonsense) [23]. Therefore, combined analyses of exome-seq and scRNA-seq could help determine the mechanism of CRACD inactivation in LUAD.

As a capping protein inhibitor, CRACD promotes actin polymerization. In colorectal cancer, CRACD inactivation disrupts the Cadherin-Catenin-Actin complex, releasing β-Catenin for WNT signaling hyperactivation [23]. However, the WNT signaling was marginally activated in *Cracd* KO lung tissues (fig. S5B), and the WNT signaling module score in the LUAD NE cluster was barely increased (fig. S5C). Thus, it is unlikely that WNT signaling mediates CRACD inactivation-induced NE plasticity. Instead, the LUAD NE tumor cell cluster displayed relatively downregulated actin-related pathways (Fig. 4C, D). Accumulating evidence suggests that actin remodeling regulates stemness and lineage commitment [44–46]. Therefore, it is probable that dysregulated actin remodeling might mediate CRACD loss-induced NE cell plasticity and increase cell de-differentiation. Mechanistically, actin cytoskeleton-driven mechanical pulling force modulates the NOTCH signaling that represses the secretory cell lineages, including the neuroendocrine cell lineage [47–51]. Additionally, nuclear actin is engaged in transcriptional regulation [52,53]. Thus, it is possible that upon CRACD inactivation, NOTCH signaling dysregulation or epigenetic reprogramming might trigger NE cell plasticity, which needs to be addressed in future studies.

While NE transformation in *EGFR* mutant or *ALK* mutant LUAD after target therapy [16,17,19] has been well known, NE transformation in *KRAS* mutant LUAD has received relatively little attention. Several case reports have recently shown that *KRAS*-mutated LUAD also transforms into NE tumor [54] and *EGFR* mutant LUAD acquires KRAS G12C mutation accompanied by NE transformation during the targeted therapy [55]. Additionally, patients of large cell neuroendocrine carcinoma (LCNEC), one of the NE tumors, harbor 22-24 % of *KRAS* mutants [56,57]. These observations imply that *KRAS* mutant LUAD might also have a potential for NE transformation, possibly by acquiring additional mutations or aberrant signaling cues that regulate cancer plasticity. Indeed, in this study, we showed that

the inactivation of CRACD, along with the mutations of *KRAS* and *TP53*, led to NE cell plasticity using animal models.

Collectively, this study reveals the crucial role of the CRACD tumor suppressor in restricting cell plasticity and cell de-differentiation, providing new insights into the NE cell plasticity of LUAD.

Limitations of the study

In our approaches, germline or somatic ablation of the *Cracd* gene, the spatiotemporal impact of *Cracd* KO on NE cell plasticity, and LUAD tumorigenesis could not be addressed. Related to this, the pathological relevance of when CRACD inactivation happens to chemotherapy resistance was not clarified, which warrants further investigation. Furthermore, the molecular mechanisms of how CRACD inactivation leads to NE cell plasticity remain to be elucidated.

STAR Methods

RESOURCE AVAILABILITY

Lead contact—Additional information and requests for resources and reagents should be directed to and will be fulfilled by the Lead Contact, Jae-Il Park (jaeil@mdanderson.org).

Materials availability—The materials will be available upon request.

Data and code availability

- scRNA-seq data are available via the Gene Expression Omnibus (GEO) and are publicly available as of the publication date. Accession numbers are listed in the Key Resource table.
- This paper does not report original code. R packages and Python packages used in this paper are listed in the Key Resource table. The code used to reproduce the analyses described in this manuscript can be accessed via Zenodo (https://doi.org/10.5281/zenodo.7843366) and is available from the lead contact upon request.
- Additional information required to reanalyze the data reported in this paper is available from the lead contact upon request.

EXPERIMENTAL MODEL AND SUBJECT DETAILS

Mice—C57BL/6, *Trp53*$^{f/f\ (floxed/floxed)}$ (JAX no. 008179), and *Kras*^{G12D} (JAX no. 008462) mice were purchased from the Jackson Laboratory. The *Cracd* KO mice were generated previously [23] using clustered regularly interspaced short palindromic repeats (CRISPR). Cas9 mRNA was purchased from Sigma Aldrich and gBlock of guide RNA (gRNA) was designed (gRNA sequence: 5′ TTCATGGGAATGGCGTTCGATGG 3′ and 5′ CAGCACAGATGCTAGCTCAGAGG 3′), based on the protospacer adjacent motif (PAM) on the target site. The gRNA was transcribed using SureGuide gRNA Synthesis Kit (Agilent). The Cas9 mRNA and gRNA were injected into the pronucleus of the C57BL/B6

blastocysts to generate *Cracd* KO mice at the genetically engineered mouse facility at the MD Anderson Cancer Center. *Kras*^{G12D}, *Trp53*$^{f/f\ (floxed/floxed)}$ (KP), *Cracd*$^{-/-}$, *Kras*^{G12D}, *Trp53*$^{f/f}$ and *Cracd*$^{+/-}$, *Kras*^{G12D}, *Trp53*$^{f/f}$ compound strains were generated by breeding, with validation of genotypes using primer sets listed in Table S1 [23,28]. For LUAD tumor induction, the lungs of 10-week-old mice were infected with adenoviral Cre (Ad-Cre) via intratracheal instillation. [28,58]. 1×10^7 PFU of virus in 50 μl of DMEM were added with $CaCl_2$ to obtain a final concentration of 10 mM and incubated for 20 minutes followed by intratracheal instillation. Multiple cohorts of independent litters were analyzed to control for background effects, and both male and female mice were used. For the KP *sgCracd* LUAD model, adenovirus containing *sgCracd*-Cre (Ad-*sgCracd*-Cre) or *sgLacZ*-Cre (Ad-*sgLacZ*-Cre; control) were introduced into KP mice via intratracheal instillation. Ad-*sgCracd*-Cre particles were produced in the Vector Development Laboratory at Baylor College of Medicine. Mice were euthanized by CO_2 asphyxiation followed by cervical dislocation at the indicated time. Tumors were harvested from euthanized mice, fixed with 10% formalin, embedded in paraffin, and sectioned at 5-μm thickness. The sections were stained with hematoxylin and eosin for histological analysis. All mice were maintained in compliance with the guidelines of the Institutional Animal Care and Use Committee of the University of Texas MD Anderson Cancer Center. All animal procedures were performed based on the guidelines of the Association for the Assessment and Accreditation of Laboratory Animal Care and institutionally approved protocols. This study was compliant with all relevant ethical regulations regarding animal research.

Lung cell isolation—Lung tissues were harvested from euthanized mice after perfusing 10 ml of cold phosphate-buffered saline (PBS) into the right ventricle. Lungs were minced after the removal of extra-pulmonary tissues and digested in Leibovitz media (Gibco, USA, no. 21083-027) with 2 mg/ml collagenase type I (Worthington, CLS-1, LS004197), 2 mg/ml elastase (Worthington, ESL, LS002294), and 0.4 mg/ml DNase I (Sigma, DN-25) for 45 minutes at 37 °C. To stop the digestion, fetal bovine serum (FBS, HyClone; Cytiva) was added to a final concentration of 20%. The digested tissues were sequentially filtered through a 70 μm and a 40 μm cell strainer (Falcon, 352350 and 352340, respectively). The samples were incubated with 1 ml of red blood cell lysis buffer (15 mM NH_4Cl, 12 mM $NaHCO_3$, 0.1 mM EDTA, pH 8.0) for 2 minutes on ice. Leibovitz with 10% FBS and 1 mM EDTA was used for resuspension and washing for magnetic-activated cell sorting (MACS).

For pulmonary epithelial cell isolation, cells were resuspended in 400 μl of buffer with 30 μl of CD31 MicroBeads (130-097-418; Miltenyi Biotec, Bergisch Gladbach, Germany), 30 μl of CD45 MicroBeads (130-052-301; Miltenyi Biotec), and 30 μl of anti-Ter-119 MicroBeads (130-049-901; Miltenyi Biotec) and incubated for 30 minutes at 4 °C, followed by negative selection according to the manufacturer's instructions. Cells were then resuspended with 400 μl of buffer with 30 μl of CD326 (EpCAM) MicroBeads (130-105-958; Miltenyi Biotec) and incubated for 30 minutes at 4 °C, followed by positive selection according to the manufacturer's instructions. Isolated lung epithelial cells were used for the lung organoid culture.

For lung endothelial cell (LuEC) isolation, cells were resuspended in 400 μl of buffer with 30 μl of CD31 MicroBeads and incubated for 30 minutes at 4 °C, followed by positive

selection according to the manufacturer's instructions. Isolated LuECs were cultured with EC growth media (DMEM; Corning; MT10013CV, 20% FBS, 1× glu-pen-strep; Gibco, USA; 10378016, 100 μg/ml endothelial cell growth factor (ECGS); Sigma; E2759, 100 μg/ml heparin; Sigma; H3149, 25 mM HEPES) on 0.1% gelatin (Sigma, G1393)-coated plates. Cultured LuECs were then isolated with CD31 MicroBeads and expanded until passage 3. Expanded LuECs were cryopreserved for lung organoid culture.

Lung organoids (LOs)—Lung epithelial cells ($Ter119^-/Cd31^-/Cd45^-/Epcam^+$) isolated from 7-10-week-old *Cracd* WT mice or *Cracd* KO were cultured with LuECs in a 3D organoid air-liquid interface [24,59]. In brief, freshly sorted lung epithelial cells were resuspended in 3D organoid media (Dulbecco's modified Eagle's medium [DMEM]/F12 [Gibco, USA]), 10% FBS [Thermo Fisher Scientific], 1× penicillin-streptomycin-glutamine [Thermo Fisher Scientific], and 1× insulin-transferrin-selenium [Thermo Fisher Scientific.]) and mixed with LuECs at a ratio of 1:1. Cells containing 3D media were mixed with growth factor-reduced Matrigel (BD Biosciences) at a ratio of 1:1. The 100 ml of mixtures containing lung epithelial cells (5×10^3) and LuECs (5×10^4) were placed in the transwell insert (0.4-mm pore, Corning, Lowell, MA). After incubation for 30 mins at 37°C in an incubator, 500 ml of 3D media was placed in the bottom chamber to generate the liquid-air interface. Media were exchanged every other day.

Mammalian cell culture—Human embryonic kidney 293T (HEK293T) and A549 cells were purchased from the American Type Culture Collection (ATCC). The murine KP-1 cells were obtained from KP mice after 12 weeks of Ad-Cre instillation [28]. HEK293T and KP-1 cells were maintained in a DMEM medium containing 10% fetal bovine serum and 1% penicillin and streptomycin. A549 cells were maintained in Roswell Park Memorial Institute (RPMI) 1640 medium containing 10% fetal bovine serum and 1% penicillin and streptomycin. Cells were cultured at 37°C in a humidified incubator supplied with 5% CO_2 air. Mycoplasma contamination was examined using the MycoAlert mycoplasma detection kit (Lonza).

METHOD DETAILS

Histology

Lung tissue: Lung tissues were perfused with cold PBS pH 7.4 into the right ventricle, fixed with 10% formalin, embedded in paraffin, and sectioned at 5-μm thickness. For H&E staining, sections were incubated in hematoxylin for 3-5 minutes and eosin Y for 20-40 s. For the immunohistochemistry analysis, sections were immunostained according to standard protocols[28]. For antigen retrieval, sections were subjected to heat-induced epitope retrieval pre-treatment at 120 °C using citrate-based antigen unmasking solution (Vector Laboratories, Burlingame, CA, USA). For immunofluorescence, after blocking with 10% goat serum in PBS for 30 minutes at ambient temperature, sections were incubated with primary antibodies (MKI67 [1:200], KRT19 [1:200], SYP [1:200], CGRP [1:200], CHGA [1:200], ASCL1 [1:200], E-Cadherin [1:200], ACTB [1:200], N-Cadherin [1:200], Vimentin [1:200], and CD44 [1:100]) overnight at 4 °C and secondary antibody (1:200) for 1 hr at ambient temperature. Sections were mounted with ProLong Gold antifade reagent with DAPI (Invitrogen). For immunohistochemistry, sections were incubated with primary

antibodies (CGRP [1:200], CHGA [1:200], and NEUROD1 [1:200]) overnight at 4 °C and secondary antibodies (1:200) for 1 hr at ambient temperature. 3,3'Diaminobenzidine (DAB) (Vector Laboratory) was used as the chromogen. Then, sections were dehydrated and mounted with Permount (Thermo Fisher Scientific). Images were captured with the fluorescence microscope (Zeiss; AxioVision). Positive areas were measured by Image J. Double-positive areas (fig. S6C, F) were measured by Image J using the BIOP JACoP plug-in [60]. See the Key Resource table for antibody information.

LOs: LOs were harvested in ice-cold PBS. Then Matrigel was removed using cell recovery solution (Corning, Lowell, MA) for 1 hr at 4°C. Collected LOs were washed with ice-cold PBS two times, fixed with 10% formalin, embedded in paraffin, and sectioned at 5-μm thickness. For H&E staining, sections were incubated in hematoxylin for 3-5 minutes and eosin Y for 20-40 s. For the immunohistochemistry analysis, sections were immunostained according to standard protocols[28]. For antigen retrieval, sections were subjected to heat-induced epitope retrieval pre-treatment at 120 °C using citrate-based antigen unmasking solution (Vector Laboratories, Burlingame, CA, USA). For immunofluorescence staining, after blocking with 10% goat serum in PBS for 30 minutes at ambient temperature, sections were incubated with primary antibodies (CGRP [1:200], CHGA [1:200], HOPX [1:100], SPC [1:200], SCGB1A1 [1:200], and Ac-Tub [1:200]) overnight at 4 °C and secondary antibody (1:200) for 1 hr at ambient temperature. Sections were mounted with ProLong Gold antifade reagent with DAPI (Invitrogen). Images were captured with the fluorescence microscope (Zeiss; AxioVision). See the Key Resource table for antibody information.

Cell lines: Cells were fixed for 20 minutes in 4% paraformaldehyde and permeabilized with 0.1% Triton X-100 (in PBS) for 10 min. After three PBS washes, cells were blocked with 2% bovine serum albumin (BSA) for 30 minutes at ambient temperature. Cells were then incubated with antibodies diluted in 2% BSA at 4°C overnight. After three PBS washes, the cells were incubated with phalloidin (Invitrogen) by shaking at ambient temperature in the dark for 1 h. Cells were washed three times with PBS in the dark and mounted in Prolong Gold Antifade Reagent (Invitrogen).

Microscopy: Immunofluorescent staining was observed and analyzed using a fluorescent microscope (ZEISS) and ZEN software (ZEISS).

Analyzing tumor heterogeneity index—Tumor heterogeneity was calculated based on the histomorphology of H&E staining. Each unique histomorphology in one tumor burden was scored as tumor heterogeneity index (Fig. S4)

Virus production and transduction—Lentiviruses were produced using the 2nd generation packaging plasmids in 293T cells. 293T cells were cultured until 70%-80% confluent, and the media were replaced with antibiotics-free DMEM (10% FBS). After 1 hour of media exchange, cells were transfected with vector mixtures in Opti-MEM (Gibco, USA). To generate a vector mixture, pMD2.G (1.3 pmol), psPAX2 (0.72 pmol), DNA (1.64 pmol), and polyethyleneimine (PEI, 39 mg) were added to 800 ml of Opti-MEM and incubated for 15 mins. After 12 hrs of transfection, the media were exchanged with complete media (DMEM, 10% FBS, and 1× penicillin-streptomycin). The virus

supernatant was collected after 24 and 48 hrs and filtered with a 0.45-mm syringe filter (Thermo Fisher, CA, USA). pLenti-shCtrl (negative silencing control; Dharmacon), pLenti-shCRACD (Dharmacon; V3LHS_367334 for generating stable cell line, V2LHS_161325 for rescue experiment), pLenti-shCracd (Dharmacon; V2LMM_57028), pLenti-GFP (W771-1; Addgene), and pLenti-3Flag-CRACD [23] plasmids were used for lentivirus generation. pLenti-GFP was a gift from Eric Campeau (Addgene plasmid # 26431; http://n2t.net/addgene:26431; RRID:Addgene_26431). A549 and KP-1 cells were transduced by lentivirus transcribing shCtrl (control) or shCRACD or shCracd, respectively, with polybrene (8 μg/ml) for 6 hours. Infected cells were selected using puromycin (2 μg/ml; Sigma) for 6 days of culture to generate stable cell lines. After generating stable cell lines, cells were cultured for 2 days without puromycin and harvested for qRT-PCR and immunoblotting analysis. For rescue experiments, shRNA-transduced stable cells were infected with lentivirus containing pLenti-GFP or pLenti-3Flag-CRACD for 12 hours and then harvested after 2 days of infection. Adenovirus containing Ad-Cre, Ad-Cre-sgLacZ, and Ad-Cre-sgCracd plasmids were generated by Gene Vector Core at BCM. See Table S1 for shRNA and sgRNA sequences.

qRT-PCR—RNAs were extracted by TRIzol (Invitrogen) and used to synthesize cDNAs using the iScript cDNA synthesis kit (Biorad). qRT-PCR was performed using an Applied Biosystems 7500 Real-Time PCR machine with the primers. Target gene expression was normalized to that of mouse *Hprt1* and human *HPRT1*. Comparative $2^{-\Delta\Delta Ct}$ methods were used to quantify qRT-PCR results. (see Table S1 for primer information).

Immunoblotting—Whole-cell lysates of mammalian cells were prepared by incubating cells with NP-40 lysis buffer (0.5% NP-40, 1.5 mM MgCl2, 25 mM HEPES, 150 mM KCl, 10% glycerol, 1 mM phenylmethylsulfonyl fluoride, 12.7 mM benzamidine HCl, 0.2 mM aprotinin, 0.5 mM leupeptin and 0.1 mM pepstatin A) for 60 minutes at 4 °C followed by centrifugation (13,148 g for 15 min). The supernatants were denatured with 5×SDS sample buffer (200 mM Tris-HCl pH 6.8, 40% glycerol, 8% SDS, 200 mM dithiothreitol and 0.08% bromophenol blue) at 95 °C for 5 minutes followed by SDS–polyacrylamide electrophoresis (SDS-PAGE). For immunoblot blocking, 2% non-fat dry milk was used in Tris-buffered saline and Tween-20 (TBST; 25 mM Tris-HCl pH 8.0, 125 mM NaCl and 0.5% Tween-20) for 1 hour at RT. For antibody incubation, 0.1% of bovine serum albumin (BSA) in TBST was used. SuperSignal West Pico (Thermo Scientific) and Femto (Thermo Scientific) reagents were used to detect horseradish peroxidase-conjugated secondary antibodies. See the Key Resource Table for antibody information.

Tumor spheroid formation assay—1×10^3 KP-1 or A549 cells in 8 μl of culture media was mixed with 12 μl of growth factor reduced Matrigel (corning). The mixture of cells with Matrigel was seeded into a 48-well culture plate. Then, Matrigel mixtures were solidified by incubating at 37 °C for 30 mins, followed by adding 500 ml of normal culture media (DMEM [10% FBS, 1% penicillin-streptomycin] for KP-1 cells and RPMI [10% FBS, 1% penicillin-streptomycin] for A549 cells. Culture media was replaced every other day. The microscope images were taken at 5 days of culture, followed by passaging. For passaging, the Matrigel mixture was washed with cold PBS and then was digested using Trypsin-EDTA

solution at 37 °C for 10 mins. After digestion, cells were suspended in culture media for passaging. Tumor spheroid formation assay was performed until control cells showed markedly reduced spheroid formation (passage 3).

Cell proliferation assay—1×10^3 KP-1 or A549 cells were seeded into a 6-well culture plate (for crystal violet staining) or 48-well staining (for proliferation assay using Ez-Cytox). For crystal violet staining, cells were stained using 0.5% crystal violet in 20% methanol. For proliferation assay, culture media was replaced with 400 μl of 10% Ez-Cytox in culture media. After 2 hours, 200 μl of media was collected, and OD (450 nm) was measured.

Wound healing assay—KP-1 or A549 cells were cultured in a 48-well culture plate until confluent. Then, cells were scratched mechanically using a 1 ml pipet tip. After 6 hours (for KP-1 cells) or 24 hours (for A549 cells) of scratch, microscope images were taken. Wound healing was measured by Image J using the wound healing size tool plug-in [61].

Drug resistance assay—1×10^3 KP-1 or A549 cells were seeded into 48-well culture plates. Cells were cultured with 1 ml of culture media containing serially diluted chemicals (range of 0.1 μM to 300 μM) for 3 days. Carboplatin (a platinum-based antineoplastic drug), gefitinib (an EGFR inhibitor), trametinib (a MEK inhibitor), and pitavastatin (an HMG-CoA inhibitor) [28] were used for drug resistance assay. After three days, culture media was replaced with 400 μl of 10% Ez-Cytox in culture media. After 2 hours, 200 μl of media was collected, and OD (450 nm) was measured.

scRNA-seq library preparation

Tissue preparation: Whole lungs were harvested from euthanized mice (Cracd WT or Cracd KO) after perfusing 10 ml of cold phosphate-buffered saline (PBS) into the right ventricle. The lung was digested in Leibovitz's medium (Invitrogen) with 2 mg/mL Collagenase Type I (Worthington), 2 mg/mL Elastase (Worthington), and 2 mg/mL DNase I (Worthington) at 37 °C for 45 min. The tissue was triturated with a pipet every 15 minutes of digestion until homogenous. The digestion was stopped with FBS (Invitrogen) to a final concentration of 20%. The cells were filtered with a 70 μm cell strainer (Falcon) and spun down at 5,000 r/min for 1 min. The cell pellet was resuspended in red blood cell lysing buffer (Sigma) for 3 min, spun down at 5,000 r/min for 1 min, and washed with 1 mL ice-cold Leibovitz's medium with 10% FBS. In single-cell RNA sequencing (scRNA-seq), digested lung cells were resuspended in 400 μl of buffer with 5 μl of anti-CD31-FITC (BD Biosciences, CA, USA), 5 μl of anti-CD45-APC (BD Biosciences), and 5 μl of anti-CD326 (EpCAM)-PE-Cy7 (Biolegend) and incubated for 30 minutes at 4 °C. Cells were then washed twice, followed by sorting of the epithelial cells (EpCAM+ / CD31-/ CD45-) by fluorescence-activated cell sorting at the Cytometry and Cell Sorting Core at the Baylor College of Medicine.

Library: The single-cell Gene Expression Library was prepared according to the guidelines for the Chromium Single Cell Gene Expression 3v3.1 kit (10X Genomics). Briefly, single cells, reverse transcription (RT) reagents, Gel Beads containing barcoded oligonucleotides, and oil were loaded on a Chromium controller (10X Genomics) to generate single-cell

GEMS (Gel Beads-In-Emulsions), where full-length cDNA was synthesized and barcoded for each single cell. Subsequently, the GEMS were broken, and cDNAs from each single cell were pooled, followed by cleanup using Dynabeads MyOne Silane Beads and cDNA amplification by PCR. The amplified product was then fragmented to optimal size before end-repair, A-tailing, and adaptor ligation. The final library was generated by amplification. The library was performed at the Single Cell Genomics Core at the Baylor College of Medicine.

scRNA-seq data analysis

Data processing, clustering, and annotation: The Cell Ranger was used for demultiplexing, barcoded processing, and gene counting. The loom files were generated using the velocyto package [62]. The R package Seurat[63] and Python package Scanpy[64] were used to pre-process and cluster scRNA-seq data with the loom files. UMAP was used for dimensional reduction, and cells were clustered in Seurat or Scanpy. Datasets were pre-processed and normalized separately. Each dataset was normalized separately and clustered by the "Leiden" algorithm [65]. *Cracd* WT and *Cracd* KO datasets were combined using the "ingest" function in Scanpy. Scanpy was used to concatenate the *Cracd* WT vs. KO dataset. Cells with more than 7000 counts reads were removed. Gene expression for each cell was normalized and log-transformed. The percentages of mitochondrial reads were regressed before scaling the data. Dimensionality reduction and Leiden clustering (resolution 0.5 ~ 1) were carried out, and cell lineages were annotated based on algorithmically defined marker gene expression for each cluster (sc.tl.rank_genes_groups, method='wilcoxon'). Each cluster-specific gene list is shown in Table S2.

Gene set enrichment analysis (GESA): AT2 cell clusters were isolated, and then the DEGs between *Cracd* KO vs. *Cracd* WT in the AT2 clusters were identified by the Wilcoxon sum test and AUROC statistics using the Presto package v. 1.0.0. They were then subjected to GSEA using the fgsea package v. 1.16.0. The curated gene sets (C5) in the Molecular Signature Database (MsigDB) v. 7.5.1 were used for the GSEA using the msigdbr package.

Pathway score analysis: Scanpy with the 'scanpy.tl.score_genes' function or Seurat with the 'AddModuleScore' function were used for the pathway score analysis. The analysis was performed with default parameters and the reference genes from the gene ontology biological process or the Kyoto Encyclopedia of Genes and Genomes database [66,67]. The gene list for the score analysis is shown in Table S3.

Cell differentiation state inference: CytoTRACE (v. 0.3.3) [26] was used to predict the relative differentiation state of a single cell.

Human scRNA-seq data analysis—The public large cohort of scRNA-seq data sets (29 datasets; 556 samples; https://doi.org/10.5281/zenodo.6411867) were downloaded and analyzed [30]. We analyzed only epithelial cell compartments (90,243 cells; 342 samples; 236 patients). The clusters were refined based on the neuroendocrine marker genes. For GSEA analysis, LUAD, LUAD mitotic, LUAD EMT, and LUAD MSLN clusters were combined

into the name of LUAD non-NE, and then GSEA of LUAD NE1 vs LUAD non-NE were analyzed as described above.

QUANTIFICATION AND STATISTICAL ANALYSIS

GraphPad Prism 9.4 (Dogmatics) was used for statistical analyses. Student's *t*-test was used to compare two samples. *P* values lower than 0.05 were considered statistically significant. Error bars indicate the standard deviation (SD) otherwise described in Figure legends. All experiments were performed three or more times independently under identical or similar conditions.

Supplementary Material

Refer to Web version on PubMed Central for supplementary material.

Acknowledgments

This work was supported by the Cancer Prevention and Research Institute of Texas (RP200315 to J.-I.P.) and the National Cancer Institute (CA193297, CA256207, CA278967, CA278971, CA279867 to J.-I.P.). The core facilities at MD Anderson (DNA Sequencing and Genetically Engineered Mouse Facility) were supported by the National Cancer Institute Cancer Center Support Grant (P30 CA016672). The core facilities at Baylor College of Medicine (Cytometry & Cell Sorting Core and Single Cell Genomics Core) were supported by CPRIT (RP180672, RP200504) and the National Institutes of Health (CA125123, RR024574).

References

1. Tata A, Chow RD, and Tata PR (2021). Epithelial cell plasticity: breaking boundaries and changing landscapes. EMBO Rep 22, e51921. 10.15252/embr.202051921. [PubMed: 34096150]
2. Nieto MA (2013). Epithelial plasticity: a common theme in embryonic and cancer cells. Science 342, 1234850. 10.1126/science.1234850. [PubMed: 24202173]
3. Scheibner K, Schirge S, Burtscher I, Büttner M, Sterr M, Yang D, Böttcher A, Ansarullah, Irmler M, Beckers J, et al. . (2021). Epithelial cell plasticity drives endoderm formation during gastrulation. Nat Cell Biol 23, 692–703. 10.1038/s41556-021-00694-x. [PubMed: 34168324]
4. Tata PR, Mou H, Pardo-Saganta A, Zhao R, Prabhu M, Law BM, Vinarsky V, Cho JL, Breton S, Sahay A, et al. . (2013). Dedifferentiation of committed epithelial cells into stem cells in vivo. Nature 503, 218–223. 10.1038/nature12777. [PubMed: 24196716]
5. Yanger K, Zong Y, Maggs LR, Shapira SN, Maddipati R, Aiello NM, Thung SN, Wells RG, Greenbaum LE, and Stanger BZ (2013). Robust cellular reprogramming occurs spontaneously during liver regeneration. Genes Dev 27, 719–724. 10.1101/gad.207803.112. [PubMed: 23520387]
6. Kusaba T, Lalli M, Kramann R, Kobayashi A, and Humphreys BD (2014). Differentiated kidney epithelial cells repair injured proximal tubule. Proc Natl Acad Sci U S A 111, 1527–1532. 10.1073/pnas.1310653110. [PubMed: 24127583]
7. Thorel F, Népote V, Avril I, Kohno K, Desgraz R, Chera S, and Herrera PL (2010). Conversion of adult pancreatic alpha-cells to beta-cells after extreme beta-cell loss. Nature 464, 1149–1154. 10.1038/nature08894. [PubMed: 20364121]
8. Tetteh PW, Basak O, Farin HF, Wiebrands K, Kretzschmar K, Begthel H, van den Born M, Korving J, de Sauvage F, van Es JH, et al. . (2016). Replacement of Lost Lgr5-Positive Stem Cells through Plasticity of Their Enterocyte-Lineage Daughters. Cell Stem Cell 18, 203–213. 10.1016/j.stem.2016.01.001. [PubMed: 26831517]
9. Mascré G, Dekoninck S, Drogat B, Youssef KK, Broheé S, Sotiropoulou PA, Simons BD, and Blanpain C (2012). Distinct contribution of stem and progenitor cells to epidermal maintenance. Nature 489, 257–262. 10.1038/nature11393. [PubMed: 22940863]
10. Painter MW, Brosius Lutz A, Cheng YC, Latremoliere A, Duong K, Miller CM, Posada S, Cobos EJ, Zhang AX, Wagers AJ, et al. . (2014). Diminished Schwann cell repair responses underlie

age-associated impaired axonal regeneration. Neuron 83, 331–343. 10.1016/j.neuron.2014.06.016. [PubMed: 25033179]

11. Torborg SR, Li Z, Chan JE, and Tammela T (2022). Cellular and molecular mechanisms of plasticity in cancer. Trends Cancer 8, 735–746. 10.1016/j.trecan.2022.04.007. [PubMed: 35618573]
12. Shi ZD, Pang K, Wu ZX, Dong Y, Hao L, Qin JX, Wang W, Chen ZS, and Han CH (2023). Tumor cell plasticity in targeted therapy-induced resistance: mechanisms and new strategies. Signal Transduct Target Ther 8, 113. 10.1038/s41392-023-01383-x. [PubMed: 36906600]
13. Meacham CE, and Morrison SJ (2013). Tumour heterogeneity and cancer cell plasticity. Nature 501, 328–337. 10.1038/nature12624. [PubMed: 24048065]
14. Rubin MA, Bristow RG, Thienger PD, Dive C, and Imielinski M (2020). Impact of Lineage Plasticity to and from a Neuroendocrine Phenotype on Progression and Response in Prostate and Lung Cancers. Mol Cell 80, 562–577. 10.1016/j.molcel.2020.10.033. [PubMed: 33217316]
15. Oser MG, Niederst MJ, Sequist LV, and Engelman JA (2015). Transformation from non-small-cell lung cancer to small-cell lung cancer: molecular drivers and cells of origin. Lancet Oncol 16, e165–172. 10.1016/s1470-2045(14)71180-5. [PubMed: 25846096]
16. Sequist LV, Waltman BA, Dias-Santagata D, Digumarthy S, Turke AB, Fidias P, Bergethon K, Shaw AT, Gettinger S, Cosper AK, et al. . (2011). Genotypic and histological evolution of lung cancers acquiring resistance to EGFR inhibitors. Sci Transl Med 3, 75ra26. 10.1126/scitranslmed.3002003.
17. Lee M, Patel D, Jofre S, Fidvi S, Suhrland M, Cohen P, and Cheng H (2022). Large Cell Neuroendocrine Carcinoma Transformation as a Mechanism of Acquired Resistance to Osimertinib in Non-small Cell Lung Cancer: Case Report and Literature Review. Clin Lung Cancer 23, e276–e282. 10.1016/j.cllc.2021.08.002. [PubMed: 34535400]
18. Awad MM, Liu S, Rybkin II, Arbour KC, Dilly J, Zhu VW, Johnson ML, Heist RS, Patil T, Riely GJ, et al. . (2021). Acquired Resistance to KRAS(G12C) Inhibition in Cancer. N Engl J Med 384, 2382–2393. 10.1056/NEJMoa2105281. [PubMed: 34161704]
19. Levacq D, D'Haene N, de Wind R, Remmelink M, and Berghmans T (2016). Histological transformation of ALK rearranged adenocarcinoma into small cell lung cancer: A new mechanism of resistance to ALK inhibitors. Lung Cancer 102, 38–41. 10.1016/j.lungcan.2016.10.012. [PubMed: 27987586]
20. Pisani D, Micallef D, Scerri J, Betts A, Degaetano J, and Baldacchino S (2023). Neuroendocrine Transdifferentiation in Cutaneous Melanoma: A Case Report and Review of the Literature. Am J Dermatopathol 45, 264–268. 10.1097/dad.0000000000002377. [PubMed: 36921302]
21. Farrell AS, Joly MM, Allen-Petersen BL, Worth PJ, Lanciault C, Sauer D, Link J, Pelz C, Heiser LM, Morton JP, et al. . (2017). MYC regulates ductal-neuroendocrine lineage plasticity in pancreatic ductal adenocarcinoma associated with poor outcome and chemoresistance. Nat Commun 8, 1728. 10.1038/s41467-017-01967-6. [PubMed: 29170413]
22. Wang Y, Wang Y, Ci X, Choi SYC, Crea F, Lin D, and Wang Y (2021). Molecular events in neuroendocrine prostate cancer development. Nat Rev Urol 18, 581–596. 10.1038/s41585-021-00490-0. [PubMed: 34290447]
23. Jung YS, Wang W, Jun S, Zhang J, Srivastava M, Kim MJ, Lien EM, Shang J, Chen J, McCrea PD, et al. . (2018). Deregulation of CRAD-controlled cytoskeleton initiates mucinous colorectal cancer via β-catenin. Nat Cell Biol 20, 1303–1314. 10.1038/s41556-018-0215-z. [PubMed: 30361697]
24. Lee JH, Bhang DH, Beede A, Huang TL, Stripp BR, Bloch KD, Wagers AJ, Tseng YH, Ryeom S, and Kim CF (2014). Lung stem cell differentiation in mice directed by endothelial cells via a BMP4-NFATc1-thrombospondin-1 axis. Cell 156, 440–455. 10.1016/j.cell.2013.12.039. [PubMed: 24485453]
25. Sánchez Alvarado A, and Yamanaka S (2014). Rethinking differentiation: stem cells, regeneration, and plasticity. Cell 157, 110–119. 10.1016/j.cell.2014.02.041. [PubMed: 24679530]
26. Gulati GS, Sikandar SS, Wesche DJ, Manjunath A, Bharadwaj A, Berger MJ, Ilagan F, Kuo AH, Hsieh RW, Cai S, et al. . (2020). Single-cell transcriptional diversity is a hallmark of developmental potential. Science 367, 405–411. 10.1126/science.aax0249. [PubMed: 31974247]

27. Ben-Porath I, Thomson MW, Carey VJ, Ge R, Bell GW, Regev A, and Weinberg RA (2008). An embryonic stem cell-like gene expression signature in poorly differentiated aggressive human tumors. Nat Genet 40, 499–507. 10.1038/ng.127. [PubMed: 18443585]
28. Kim MJ, Cervantes C, Jung YS, Zhang X, Zhang J, Lee SH, Jun S, Litovchick L, Wang W, Chen J, et al. . (2021). PAF remodels the DREAM complex to bypass cell quiescence and promote lung tumorigenesis. Mol Cell 81, 1698–1714.e1696. 10.1016/j.molcel.2021.02.001. [PubMed: 33626321]
29. Kim KB, Kabra A, Kim DW, Xue Y, Huang Y, Hou PC, Zhou Y, Miranda LJ, Park JI, Shi X, et al. . (2022). KIX domain determines a selective tumor-promoting role for EP300 and its vulnerability in small cell lung cancer. Sci Adv 8, eabl4618. 10.1126/sciadv.abl4618. [PubMed: 35171684]
30. Salcher S, Sturm G, Horvath L, Untergasser G, Kuempers C, Fotakis G, Panizzolo E, Martowicz A, Trebo M, Pall G, et al. . (2022). High-resolution single-cell atlas reveals diversity and plasticity of tissue-resident neutrophils in non-small cell lung cancer. Cancer Cell 40, 1503–1520.e1508. 10.1016/j.ccell.2022.10.008. [PubMed: 36368318]
31. Reya T, and Clevers H (2005). Wnt signalling in stem cells and cancer. Nature 434, 843–850. 10.1038/nature03319. [PubMed: 15829953]
32. Nieto MA, Huang RY, Jackson RA, and Thiery JP (2016). EMT: 2016. Cell 166, 21–45. 10.1016/j.cell.2016.06.028. [PubMed: 27368099]
33. Williams ED, Gao D, Redfern A, and Thompson EW (2019). Controversies around epithelial-mesenchymal plasticity in cancer metastasis. Nat Rev Cancer 19, 716–732. 10.1038/s41568-019-0213-x. [PubMed: 31666716]
34. Fischer KR, Durrans A, Lee S, Sheng J, Li F, Wong ST, Choi H, El Rayes T, Ryu S, Troeger J, et al. . (2015). Epithelial-to-mesenchymal transition is not required for lung metastasis but contributes to chemoresistance. Nature 527, 472–476. 10.1038/nature15748. [PubMed: 26560033]
35. Zheng X, Carstens JL, Kim J, Scheible M, Kaye J, Sugimoto H, Wu CC, LeBleu VS, and Kalluri R (2015). Epithelial-to-mesenchymal transition is dispensable for metastasis but induces chemoresistance in pancreatic cancer. Nature 527, 525–530. 10.1038/nature16064. [PubMed: 26560028]
36. Yuan TC, Veeramani S, and Lin MF (2007). Neuroendocrine-like prostate cancer cells: neuroendocrine transdifferentiation of prostate adenocarcinoma cells. Endocr Relat Cancer 14, 531–547. 10.1677/erc-07-0061. [PubMed: 17914087]
37. Reya T, Morrison SJ, Clarke MF, and Weissman IL (2001). Stem cells, cancer, and cancer stem cells. Nature 414, 105–111. 10.1038/35102167. [PubMed: 11689955]
38. Hanahan D (2022). Hallmarks of Cancer: New Dimensions. Cancer Discov 12, 31–46. 10.1158/2159-8290.CD-21-1059. [PubMed: 35022204]
39. Gardner EE, Lok BH, Schneeberger VE, Desmeules P, Miles LA, Arnold PK, Ni A, Khodos I, de Stanchina E, Nguyen T, et al. . (2017). Chemosensitive Relapse in Small Cell Lung Cancer Proceeds through an EZH2-SLFN11 Axis. Cancer Cell 31, 286–299. 10.1016/j.ccell.2017.01.006. [PubMed: 28196596]
40. George J, Lim JS, Jang SJ, Cun Y, Ozretic L, Kong G, Leenders F, Lu X, Fernandez-Cuesta L, Bosco G, et al. . (2015). Comprehensive genomic profiles of small cell lung cancer. Nature 524, 47–53. 10.1038/nature14664. [PubMed: 26168399]
41. Rudin CM, Durinck S, Stawiski EW, Poirier JT, Modrusan Z, Shames DS, Bergbower EA, Guan Y, Shin J, Guillory J, et al. . (2012). Comprehensive genomic analysis identifies SOX2 as a frequently amplified gene in small-cell lung cancer. Nat Genet 44, 1111–1116. 10.1038/ng.2405. [PubMed: 22941189]
42. Gay CM, Stewart CA, Park EM, Diao L, Groves SM, Heeke S, Nabet BY, Fujimoto J, Solis LM, Lu W, et al. . (2021). Patterns of transcription factor programs and immune pathway activation define four major subtypes of SCLC with distinct therapeutic vulnerabilities. Cancer Cell 39, 346–360 e347. 10.1016/j.ccell.2020.12.014. [PubMed: 33482121]
43. Zhang S, Kim KB, Huang Y, Kim DW, Kim B, Ko KP, Zou G, Zhang J, Jun S, Kirk NA, et al. . (2023). CRACD loss promotes small cell lung cancer tumorigenesis via EZH2-mediated immune evasion. bioRxiv. 10.1101/2023.02.15.528365.

44. Fletcher DA, and Mullins RD (2010). Cell mechanics and the cytoskeleton. Nature 463, 485–492. 10.1038/nature08908. [PubMed: 20110992]
45. Davidson PM, and Cadot B (2021). Actin on and around the Nucleus. Trends Cell Biol 31, 211–223. 10.1016/j.tcb.2020.11.009. [PubMed: 33376040]
46. Guo J, Wang Y, Sachs F, and Meng F (2014). Actin stress in cell reprogramming. Proc Natl Acad Sci U S A 111, E5252–5261. 10.1073/pnas.1411683111. [PubMed: 25422450]
47. Luca VC, Kim BC, Ge C, Kakuda S, Wu D, Roein-Peikar M, Haltiwanger RS, Zhu C, Ha T, and Garcia KC (2017). Notch-Jagged complex structure implicates a catch bond in tuning ligand sensitivity. Science 355, 1320–1324. 10.1126/science.aaf9739. [PubMed: 28254785]
48. Wang X, and Ha T (2013). Defining single molecular forces required to activate integrin and notch signaling. Science 340, 991–994. 10.1126/science.1231041. [PubMed: 23704575]
49. Gordon WR, Zimmerman B, He L, Miles LJ, Huang J, Tiyanont K, McArthur DG, Aster JC, Perrimon N, Loparo JJ, and Blacklow SC (2015). Mechanical Allostery: Evidence for a Force Requirement in the Proteolytic Activation of Notch. Dev Cell 33, 729–736. 10.1016/j.devcel.2015.05.004. [PubMed: 26051539]
50. Meloty-Kapella L, Shergill B, Kuon J, Botvinick E, and Weinmaster G (2012). Notch ligand endocytosis generates mechanical pulling force dependent on dynamin, epsins, and actin. Dev Cell 22, 1299–1312. 10.1016/j.devcel.2012.04.005. [PubMed: 22658936]
51. Quintanal-Villalonga A, Taniguchi H, Zhan YA, Hasan MM, Chavan SS, Meng F, Uddin F, Manoj P, Donoghue MTA, Won HH, et al. (2021). Multiomic Analysis of Lung Tumors Defines Pathways Activated in Neuroendocrine Transformation. Cancer Discov 11, 3028–3047. 10.1158/2159-8290.Cd-20-1863. [PubMed: 34155000]
52. Huang Y, Zhang S, and Park JI (2022). Nuclear Actin Dynamics in Gene Expression, DNA Repair, and Cancer. Results Probl Cell Differ 70, 625–663. 10.1007/978-3-031-06573-6_23. [PubMed: 36348125]
53. Olave IA, Reck-Peterson SL, and Crabtree GR (2002). Nuclear actin and actin-related proteins in chromatin remodeling. Annu Rev Biochem 71, 755–781. 10.1146/annurev.biochem.71.110601.135507. [PubMed: 12045110]
54. Ito T, Oi I, Saito Z, Imakita T, Kanai O, Fujita K, Tachibana H, Moriyoshi K, and Mio T (2023). De Novo SCLC Transformation From KRAS G12C-Mutated Lung Adenocarcinoma With Excellent Response to Sotorasib: A Case Report. JTO Clin Res Rep 4, 100510. 10.1016/j.jtocrr.2023.100510. [PubMed: 37131995]
55. Gu Y, Zhu X, Cao B, Wu X, Tong X, Shao YW, and Liang L (2019). Transformation to small cell lung cancer and activation of KRAS during long-term erlotinib maintenance in a patient with non-small cell lung cancer: A case report. Oncol Lett 17, 5219–5223. 10.3892/ol.2019.10196. [PubMed: 31186738]
56. Naidoo J, Santos-Zabala ML, Iyriboz T, Woo KM, Sima CS, Fiore JJ, Kris MG, Riely GJ, Lito P, Iqbal A, et al. . (2016). Large Cell Neuroendocrine Carcinoma of the Lung: Clinico-Pathologic Features, Treatment, and Outcomes. Clin Lung Cancer 17, e121–e129. 10.1016/j.cllc.2016.01.003. [PubMed: 26898325]
57. Rekhtman N, Pietanza MC, Hellmann MD, Naidoo J, Arora A, Won H, Halpenny DF, Wang H, Tian SK, Litvak AM, et al. (2016). Next-Generation Sequencing of Pulmonary Large Cell Neuroendocrine Carcinoma Reveals Small Cell Carcinoma-like and Non-Small Cell Carcinoma-like Subsets. Clin Cancer Res 22, 3618–3629. 10.1158/1078-0432.Ccr-15-2946. [PubMed: 26960398]
58. DuPage M, Dooley AL, and Jacks T (2009). Conditional mouse lung cancer models using adenoviral or lentiviral delivery of Cre recombinase. Nature protocols 4, 1064–1072. [PubMed: 19561589]
59. Dost AFM, Moye AL, Vedaie M, Tran LM, Fung E, Heinze D, Villacorta-Martin C, Huang J, Hekman R, Kwan JH, et al. . (2020). Organoids Model Transcriptional Hallmarks of Oncogenic KRAS Activation in Lung Epithelial Progenitor Cells. Cell Stem Cell 27, 663–678.e668. 10.1016/j.stem.2020.07.022. [PubMed: 32891189]
60. Bolte S, and Cordelières FP (2006). A guided tour into subcellular colocalization analysis in light microscopy. J Microsc 224, 213–232. 10.1111/j.1365-2818.2006.01706.x. [PubMed: 17210054]

61. Suarez-Arnedo A, Torres Figueroa F, Clavijo C, Arbeláez P, Cruz JC, and Muñoz-Camargo C (2020). An image J plugin for the high throughput image analysis of in vitro scratch wound healing assays. PLoS One 15, e0232565. 10.1371/journal.pone.0232565. [PubMed: 32722676]

62. La Manno G, Soldatov R, Zeisel A, Braun E, Hochgerner H, Petukhov V, Lidschreiber K, Kastriti ME, Lönnerberg P, Furlan A, et al. . (2018). RNA velocity of single cells. Nature 560, 494–498. 10.1038/s41586-018-0414-6. [PubMed: 30089906]

63. Hao Y, Hao S, Andersen-Nissen E, Mauck III WM, Zheng S, Butler A, Lee MJ, Wilk AJ, Darby C, and Zager M (2021). Integrated analysis of multimodal single-cell data. Cell 184, 3573–3587. e3529. [PubMed: 34062119]

64. Wolf FA, Angerer P, and Theis FJ (2018). SCANPY: large-scale single-cell gene expression data analysis. Genome Biology 19, 15. 10.1186/s13059-017-1382-0. [PubMed: 29409532]

65. Traag VA, Waltman L, and Van Eck NJ (2019). From Louvain to Leiden: guaranteeing well-connected communities. Scientific reports 9, 1–12. [PubMed: 30626917]

66. Kanehisa M (1996). Toward pathway engineering: a new database of genetic and molecular pathways. Sci. Technol. Jap. 59, 34–38.

67. Ashburner M, Ball CA, Blake JA, Botstein D, Butler H, Cherry JM, Davis AP, Dolinski K, Dwight SS, Eppig JT, et al. . (2000). Gene ontology: tool for the unification of biology. The Gene Ontology Consortium. Nat Genet 25, 25–29. 10.1038/75556. [PubMed: 10802651]

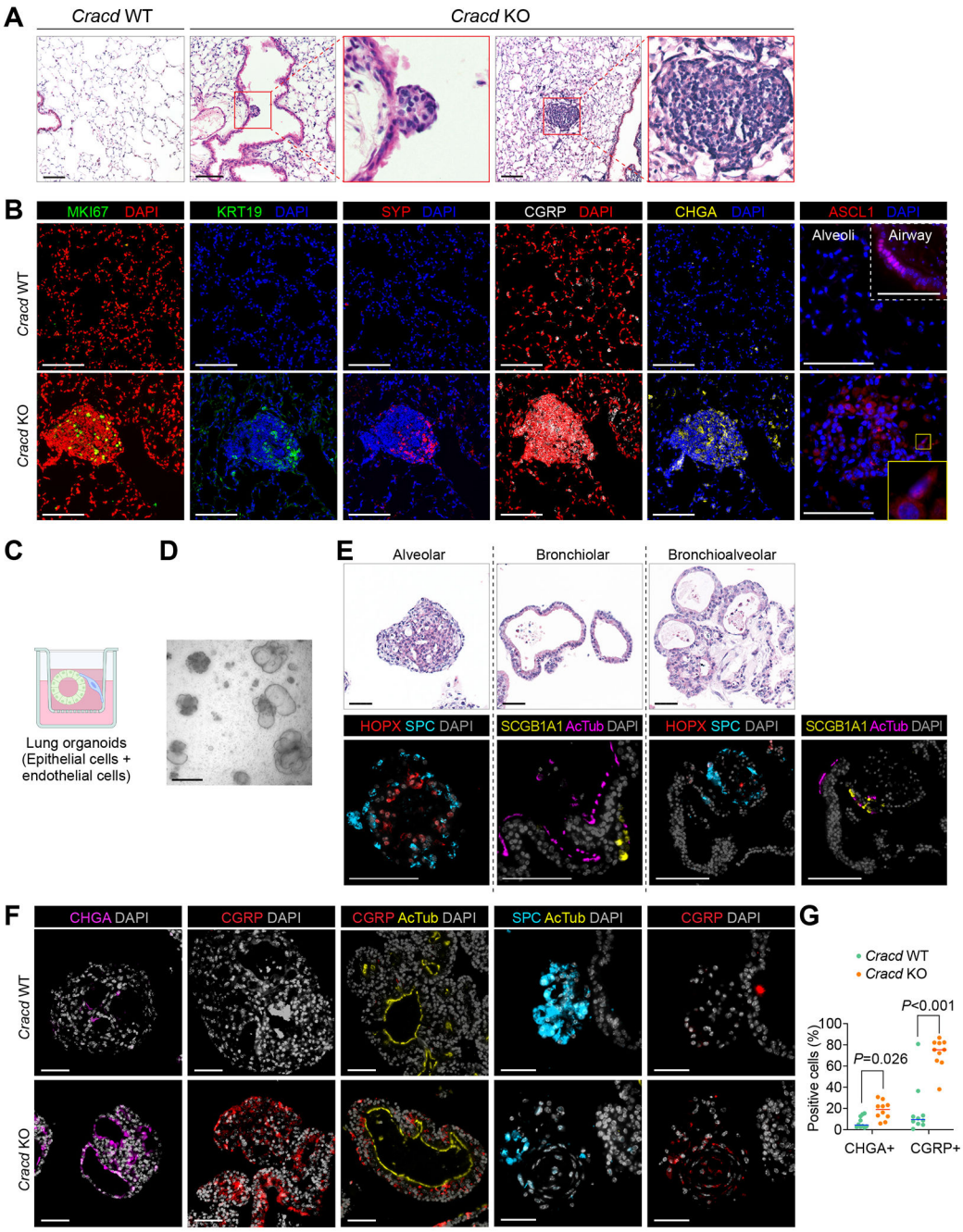

Figure 1. *Cracd* KO induces NE cell-like features in the pulmonary epithelium and organoids.

A, B, Hematoxylin and eosin (H&E) (A) and immunofluorescent (IF) (B) staining of mouse lung sections (*Cracd* WT vs. KO) (n = 3 per group); scale bars, 100μm.

C, Illustration of lung organoid (Lo) culture.

D, Bright-field images of LOs at day 12; scale bars, 500μm.

E, H&E (upper panels) and IF (lower panels) staining of LOs; scale bars, 100μm.

F, IF staining of LOs derived from *Cracd* WT vs. KO mice; scale bars, 50μm.

G, Quantification of CHGA+ and CGRP+ cells in LOs (n = 10 per Lo). Two-tailed Student's *t*-test; error bars: SD.

Representative images were displayed.

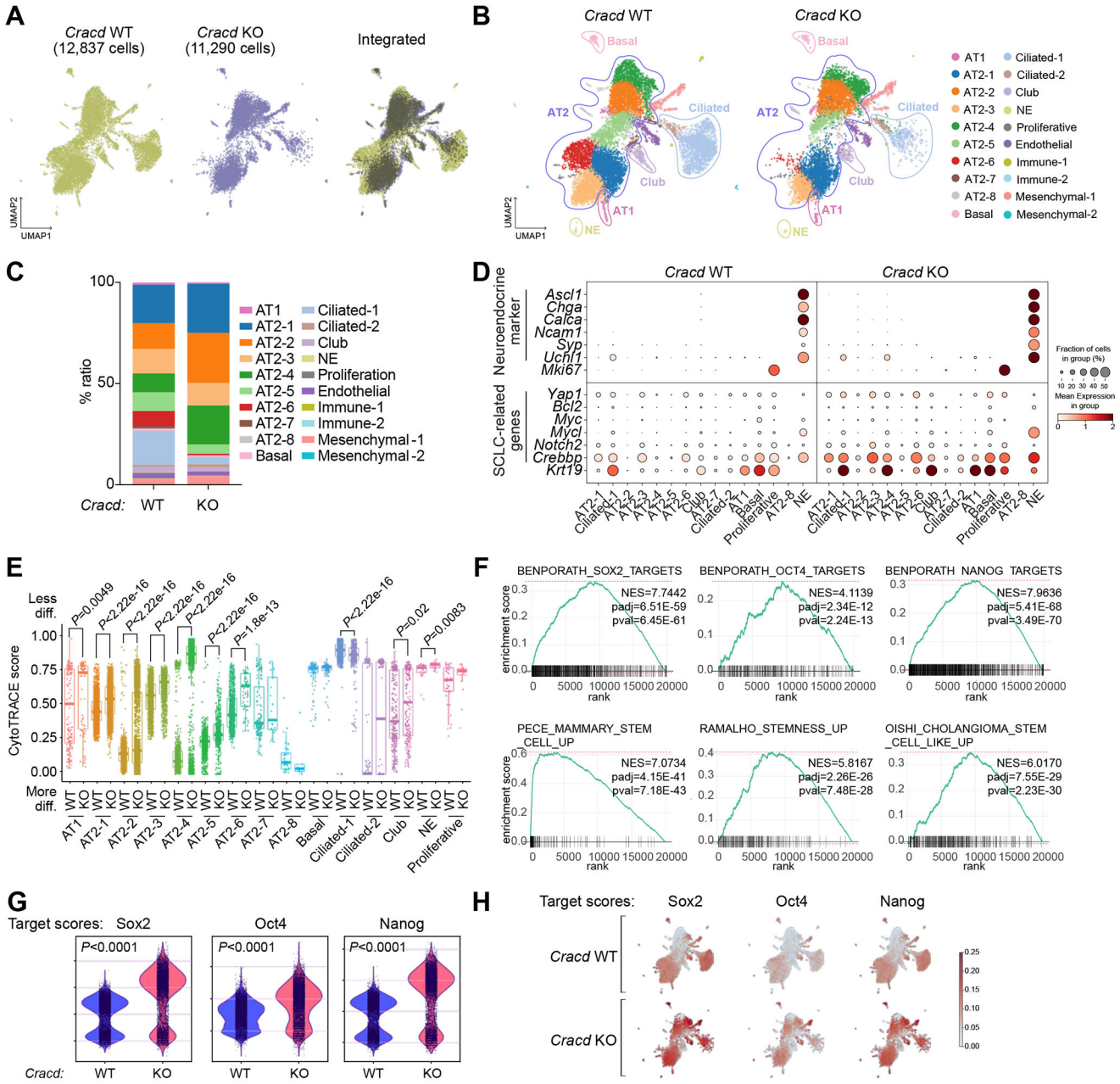

Figure 2. *Cracd* KO drives de-differentiation-like features in the alveolar cells.

A, Uniform manifold approximation and projection (UMAP) plots displaying pulmonary epithelial cells from *Cracd* WT vs. KO mice.

B, UMAPs of each cell cluster annotated by cell types.

C, Bar plot displaying cell proportion of each cell type shown in Figure 2B.

D, Dot plots showing the expression of NE- and SCLC-related genes split by *Cracd* genotype.

E, Boxplots of CytoTRACE scores of each cell cluster; less/more diff: less/more differentiated cell states.

F, GSEA of the AT2 clusters (*Cracd* WT vs. KO) using the datasets shown in Figure 4A.
G, Dot plots depicting transcriptional module scores of Sox2, Oct4, and Nanog in the AT2 clusters.
H, Feature plots showing the module scores (Sox2, Oct4, and Nanog).

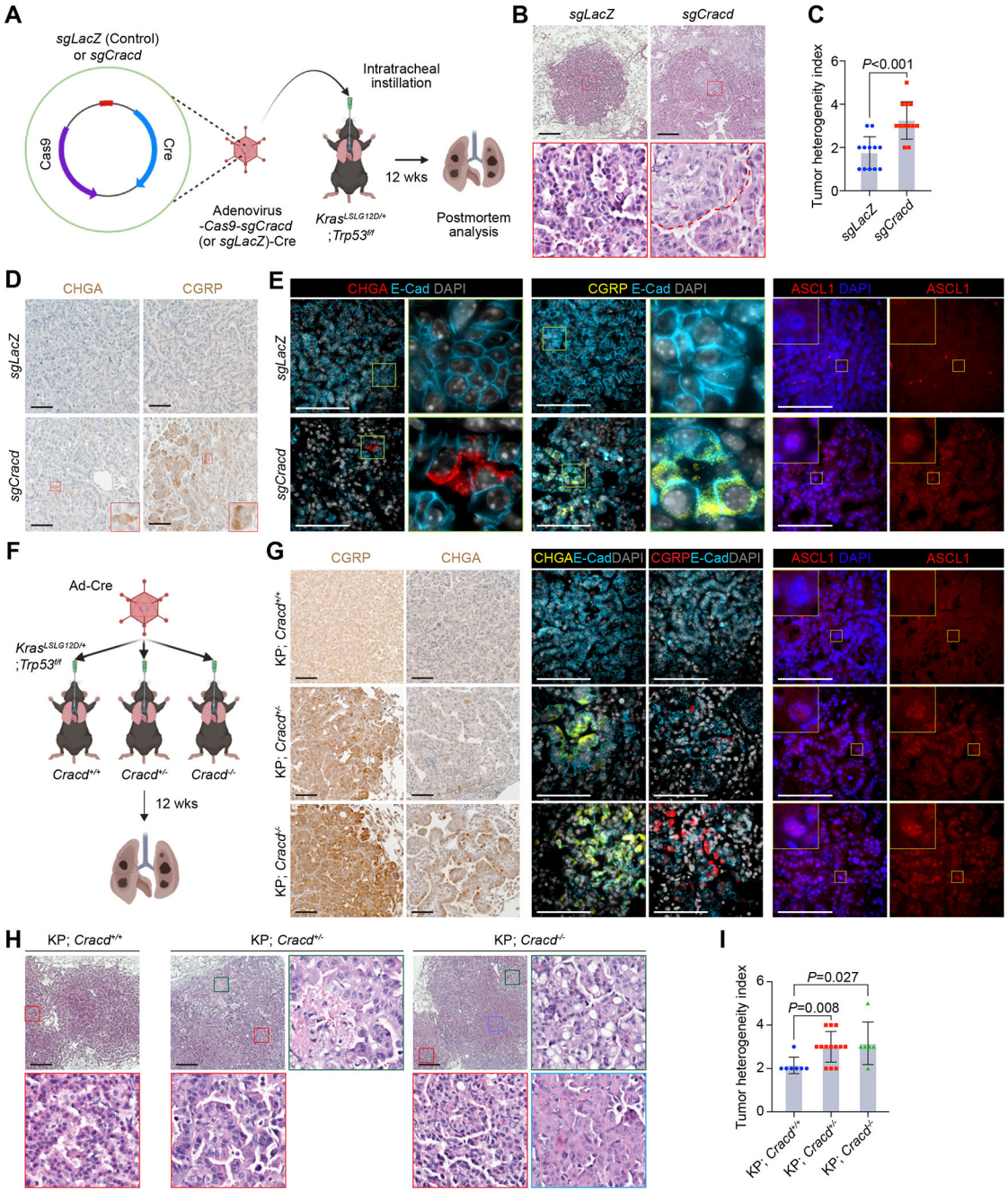

Figure 3. *Cracd* KO increases tumor heterogeneity with NE gene expression in LUAD mouse models.

A, Illustration of somatic gene targeting using adenovirus encoding sgRNAs and Cre; (n = 3 per group).

B, C, Tumor heterogeneity analysis; H&E (B); intratumoral heterogeneity index (C) (n = 12 per group); scale bars, 400μm.

D, E, Immunostaining of lung tumors; DAB (3,3'-Diaminobenzidine) (D); IF (E); scale bars, 100μm.

F, Experimental scheme of Cracd-deficient LUAD mice model using *Cracd* germline KO mice.

G, Immunostaining of lung tumors; DAB or IF; scale bars, 100μm.

H, I, Tumor heterogeneity analysis; H&E (H); intratumoral heterogeneity index (I); *Cracd* WT (n = 3) vs. *Cracd* KO (heterozygous [n=11] vs. homozygous [n=2]); scale bars, 400μm. Representative images were shown. Two-tailed Student's *t*-test; error bars: SD.

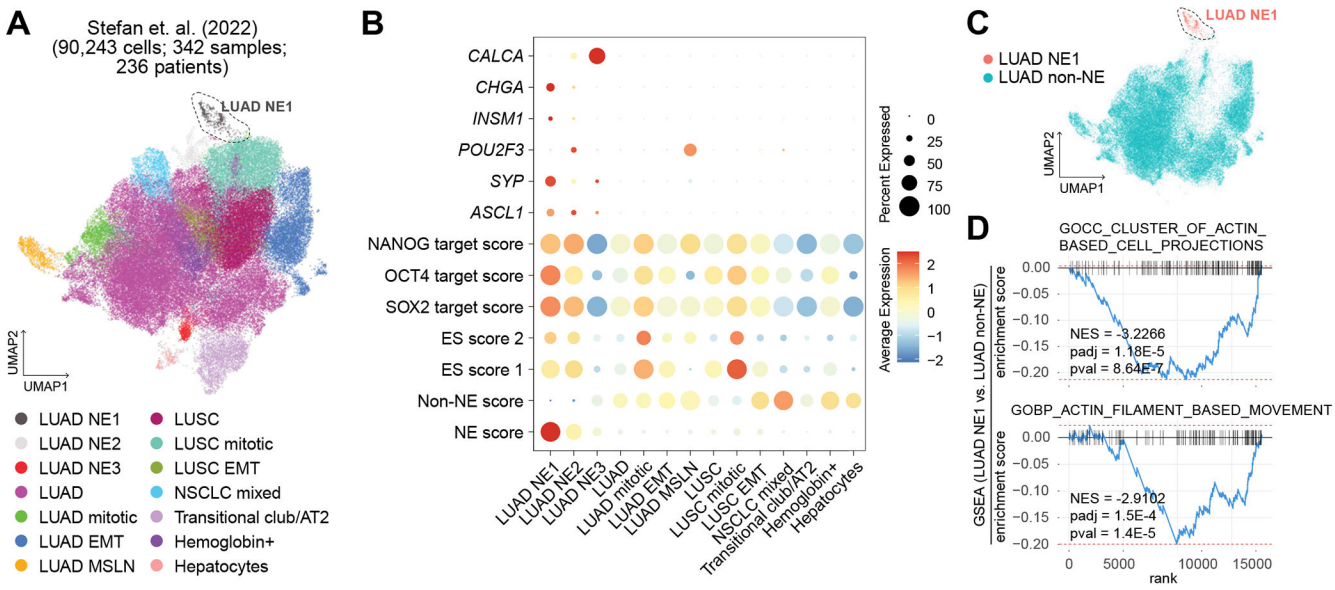

Figure 4. Association of NE cell plasticity with cell stemness in LUAD patients.

A, UMAP of scRNA-seq datasets of NSCLC tumor cells annotated by tumor cell types.

B, Dot plot depicting NE gene expression and transcriptional module scores of the gene sets.

C, UMAP displaying the two subsets (LUAD NE1 vs. LUAD non-NE [LUAD, LUAD mitotic, LUAD EMT, and LUAD MSLN]).

D, GSEA of LUAD NE1 vs. LUAD non-NE.

KEY RESOURCES TABLE

REAGENT or RESOURCE	SOURCE	IDENTIFIER
Antibodies		
Rabbit anti-Ki67 (MKI67)	Abcam	Cat# ab16667; RRID:AB_302459
Mouse anti-Cytokeratin 19 (KRT19)	Abcam	Cat# ab194399; RRID:AB 2936398
Rabbit anti- Synaptophysin (SYP)	Cell Signaling	Cat# 36406; RRID: AB 2799098
Rabbit anti-CGRP	Immunostar	Cat# 24112; RRID: AB 572217
Rabbit anti-Chromogranin A (CHGA)	Abcam	Cat# ab15160; RRID: AB 301704
Mouse anti-Hop (HOPX)	SantaCruz	Cat# sc-398703; RRID: AB 2687966
Rabbit anti-Prosurfactant Protein C (SPC)	Abcam	Cat# ab40879; RRID: AB 777473
Rabbit anti-Uteroglobin (SCGB1A1)	Abcam	Cat# ab40873; RRID: AB 778766
Mouse anti-Tubulin, Acetylated (Ac-Tub)	Sigma	Cat# T6793; RRID: AB 477585
Mouse anti-E-cadherin	Cell Signaling	Cat# 14472; RRID: AB 2728770
Mouse anti-Beta Actin (ACTB)	Proteintech	Cat# 66009–1-Ig; RRID: AB 2687938
Rabbit anti-MASH1 (ASCL1)	Abcam	Cat# ab211327; RRID: AB 2924270
Goat anti-NEUROD1	Invitrogen	Cat# PA5-47381; RRID: AB 2607915
Rat anti-CD31 MicroBeads, mouse	Miltenyi Biotec	Cat# 130-097-418; RRID: AB 2814657
Rat anti-CD326 (EPCAM) MicroBeads, mouse	Miltenyi Biotec	Cat# 130-105-958; RRID: AB 2936423
Rat anti-TER-119 MicroBeads, mouse	Miltenyi Biotec	Cat# 130-049-901; RRID: AB 2936424
Rat anti-CD45 MicroBeads, mouse	Miltenyi Biotec	Cat# 130-052-301; RRID: AB 2877061
Rat anti-CD31 FITC	BD Biosciences	Cat# 553372; RRID: AB 394818
Rat anti-CD45 APC	BD Biosciences	Cat# 559864; RRID: AB 398672
Rat anti-CD326 (EPCAM) PE/Cy7	BioLegend	Cat# 118216; RRID: AB 1236471
Mouse anti-Vimentin	BD Biosciences	Cat# 550513; RRID: AB_393716
Mouse anti-N-Cadherin	BD Biosciences	Cat# 610921; RRID: AB_398236
Rabbit anti-CRAD (CRACD)	Invitrogen	Cat# PA5-61669; RRID: AB_2643037
Rabbit anti-UCHL1	Cell Signaling	Cat# 13179; RRID: AB_2798141
Rabbit anti-GAPDH	Cell Signaling	Cat# 5174S; RRID: AB_10622025
Rat anti-CD44	BD Biosciences	Cat# 550538; RRID: AB_393732
Rabbit anti-SOX2	Cell Signaling	Cat# 14962; RRID: AB_2798664
Rabbit anti-OCT4 (POU5F1)	Abcam	Cat# ab19857; RRID: AB_445175
Rabbit anti-NANOG	Novus	Cat# NB100-58842; RRID: AB_877697
Bacterial and virus strains		
Ad-Cre	BCM Gene Vector Core	N/A
Ad-Cre-sgLacZ	BCM Gene Vector Core	N/A
Ad-Cre-sgCracd	BCM Gene Vector Core	N/A
Chemicals, peptides, and recombinant proteins		
Fetal Bovine Serum	Thermo Fisher Scientific	Cat# SH3091003
Dulbecco’s modified Eagle’s medium [DMEM]	Thermo Fisher Scientific	Cat# MT10013CV

REAGENT or RESOURCE	SOURCE	IDENTIFIER
advanced DMEM/F12	Thermo Fisher Scientific	Cat# 12634010
Roswell Park Memorial Institute (RPMI) 1640 medium	Thermo Fisher Scientific	Cat# MT10040CV
Leibovitz's L-15 Medium, no phenol red	Thermo Fisher Scientific	Cat# 21083027
Opti-MEM™ I Reduced Serum Medium	Thermo Fisher Scientific	Cat# 31985070
0.05% trypsin-EDTA	Thermo Fisher Scientific.	Cat# 25-052-CI
penicillin/streptomycin	Life Technologies	Cat# 15140122
100× GlutaMAX™	Life Technologies	Cat# 35050061
Penicillin-Streptomycin-Glutamine (100X)	Thermo Fisher Scientific.	Cat# 10378016
Collagenase, Type 1	Worthington	Cat# LS004197
Elastase	Worthington	Cat# LS002294
Deoxyribonuclease I from bovine pancreas	Sigma	Cat# DN-25
Endothelial Cell Growth Supplement (ECGS)	Sigma	Cat# 02-102
Heparin sodium salt from porcine intestinal mucosa	Sigma	Cat# H3149
Gelatin solution	Sigma	Cat# G1393
Insulin-Transferrin-Selenium (ITS -G) (100X)	Thermo Fisher Scientific.	Cat# 41400045
Matrigel	Corning	Cat# 356231
TRIzol Reagent	Thermo Fisher Scientific.	Cat# 15596026
iScript™ cDNA Synthesis Kit	BioRad	Cat# 1708891
Harris' Hematoxylin (for H&E)	National Diagnostics	Cat# HS-400
Eosin Solution	National Diagnostics	Cat# HS-402
Antigen Unmasking Solution, Citrate-Based	Vector Laboratories	Cat# H3300
ImmPACT® DAB Substrate Kit, Peroxidase (HRP)	Vector Laboratories	Cat# SK-4105
ProLong™ Gold Antifade Mountant with DNA Stain DAPI	Thermo Fisher Scientific.	Cat# P36935
Permount™ Mounting Medium	Thermo Fisher Scientific.	Cat# SP15
Cell Recovery Solution	Corning	Cat# 354253
Alexa Fluor™ 488 Phalloidin	Thermo Fisher Scientific.	Cat# A12379
puromycin	Sigma	Cat# P8833-100MG
Polybrene Infection / Transfection Reagent	Sigma	Cat# TR-1003-G
Polyethyleneimine, linear, M.W. 25,000	Thermo Fisher Scientific.	Cat# AA4389603
5-Bromo-2'-deoxyuridine (BrdU)	Cayman	Cat# 15580
Matrigel GFR, Phenol Red-free, LDEV-free	Corning	Cat# 356231
Ez-Cytox	DoGenGio	Cat# EZ-3000
Carboplatin	Selleckchem	Cat# S1215
Gefitinib	SantaCruz	Cat# sc-202166
Trametinib	Cayman Chemical	Cat# 16292
Pitavastatin	Selleckchem	Cat# S1759
Deposited data		
Cracd WT and Cracd KO scRNA-seq dataset	This paper	GEO: GSE229982

REAGENT or RESOURCE	SOURCE	IDENTIFIER
Human lung cancer scRNA-seq dataset	Salcher et al. [30]	https://doi.org/10.5281/zenodo.6411867
Experimental models: Cell lines		
HEK293T	ATCC	CRL-3216
A549	ATCC	CRM-CCL-185
KP-1	Kim et al. [25]	N/A
Experimental models: Organisms/strains		
Mouse: C57BL/6J	The Jackson Laboratory	JAX: 000664; RRID: IMSR_JAX:000664
Mouse: B6.129S4-Krastm4Tyj/J	The Jackson Laboratory	JAX: 008179; RRID:IMSR_JAX:007676
Mouse: B6.129P2-Trp53tm1Brn/J	The Jackson Laboratory	JAX: 008462; RRID: IMSR_JAX:008462Info
Mouse: C57BL/6J. Cracd KO	Jung et al. [23]	N/A
Oligonucleotides		
Primers for genotyping, qPCR, see Table S1	Previously	N/A
Recombinant DNA		
psPAX2	Addgene	Addgene #12260
pMD2.G	Addgene	Addgene #12259
SMARTvector Lentiviral Controls	Dharmacon	Cat# VSC11707
GIPZ Lentiviral Human KIAA1211 (CRACD) shRNA	Dharmacon	Clone id V3LHS_367334
GIPZ Lentiviral Mouse C530008M17Rik (Cracd) shRNA	Dharmacon	Clone id V2LMM_57028
GIPZ Lentiviral Human KIAA1211 (CRACD) shRNA (Targeting 3' UTR; used for rescue experiment)	Dharmacon	Clone id V2LHS_161325
pLenti-3Flag-CRACD	Jung et al. [23]	DOI: 10.1038/s41556-018-0215-z
pLenti-GFP	Addgene	Addgene #26431
Software and algorithms		
Codes used for scRNA-seq analysis using packages listed below are available on zenodo	This study	https://doi.org/10.5281/zenodo.7843366
CellRanger (v3.1.0)	10x Genomics	https://support.10xgenomics.com/single-cell-gene-expression/software/downloads/latest
R (v4.0.3)	N/A	http://www.r-project.org/
R Studio (v1.4.1106)	N/A	https://www.rstudio.com/
Seurat (v4.0.3)	Hao et al. [63]	https://satijalab.org/seurat/
BiocManager (v1.30.16)	N/A	https://www.bioconductor.org/
fgsea (v1.16.0)	N/A	https://bioconductor.org/packages/release/bioc/html/fgsea.html
presto (v1.0.0)	N/A	https://github.com/immunogenomics/presto
Python (3.8.12)	N/A	https://www.python.org/
Velocyto (v.0.17.17)	La Manno et al. [62]	https://pypi.org/project/velocyto/
Scanpy (v1.8.2)	Wolf et al. [64]	https://scanpy.readthedocs.io/en/stable/#
Loompy (v3.0.6)	N/A	https://linnarssonlab.org/loompy/
CytoTRACE (v.0.3.3)	Gulati et al. [26]	https://cytotrace.stanford.edu/
fgsea (v1.16.0)	N/A	https://www.bioconductor.org/

REAGENT or RESOURCE	SOURCE	IDENTIFIER
MsigDB (v.7.5.1)	N/A	https://bioconductor.org/packages/release/data/experiment/html/msigdb.html
ImageJ	ImageJ	https://imagej.nih.gov/ij/
ImageJ plug-in [Wound healing size tool]	Suarez-Arnedo et al. [61]	https://github.com/AlejandraArnedo/Wound-healing-size-tool/wiki#wound-healing-size-tool
ImageJ plug-in [BIOP JACoP]	Bolte et al. [60]	https://github.com/BIOP/ijp-jacop-b
GraphPad Prism 9.4	Graphpad	https://www.graphpad.com/scientificsoftware/prism/